Optimal balance for rotating shallow water in primitive variables

Gökce Tuba Masur and Marcel Oliver

School of Engineering and Science, Jacobs University, 28759 Bremen, Germany

ARTICLE HISTORY
Compiled March 18, 2020

ABSTRACT
Optimal balance is a near-optimal computational algorithm for nonlinear mode decomposition of geophysical flows into balanced and unbalanced components. It was first proposed as "optimal potential vorticity balance" by Viúdez and Dritschel (*J. Fluid Mech.*, 2004, **521**, 343) in the specific setting of semi-Lagrangian potential vorticity-based numerical codes. Later, it was recognized as an instance of the more general principle of adiabatic invariance of fast degrees of motion under slow perturbations. From this point of view, the system is slowly deformed from a linearized configuration to the full nonlinear dynamics. In the former, linear analysis yields an exact separation of balanced and unbalanced flow. In the latter, a given base-point coordinate, e.g. the height or potential vorticity field, can be matched. This formulation leads to a boundary value problem in time.

In this paper, we show that this more general viewpoint leads to practical implementations of optimal balance on top of a primitive variables (here, velocity-height variables) numerical code. We identify preferred choices for several design parameters. The most critical choices concern the linear projector onto the slow modes at the linear-end boundary and the choice of base-point coordinate at the nonlinear end. We find that, even though the evolutionary model is formulated in primitive variables, potential vorticity based end-point conditions are advantageous. In particular, the only universally robust linear projector is the oblique projector onto the Rossby modes along the gravity wave modes, which can be interpreted as the distinct non-orthogonal projector onto the Rossby modes that preserves the linear potential vorticity. Hence, the projector can be formulated as an elliptic partial differential equation which holds promise for using the method to produce an accurate nonlinear mode decomposition for more general models without the need to resort to asymptotic analysis.

KEYWORDS
nonlinear mode decomposition, adiabatic invariance, rotating shallow water equations, linear potential vorticity, oblique projector

1. Introduction

Geophysical fluid flow at mid-latitudes is dominated by an approximate balance between the pressure gradient force with the Coriolis force in the horizontal, and hydrostatic balance in the vertical. For the linearized equations of motion, it is possible to decompose the solution exactly into normal modes which can be classified into Rossby modes and gravity modes, or slow and fast modes, the latter characterized by their asymptotics as the Coriolis and stratification parameters get large. (For global models, the situation is more complicated due to the existence of mixed Rossby-gravity waves and equatorial Kelvin waves which shall not be discussed further in this paper.) For

the full nonlinear dynamics, however, an exact decomposition is impossible. In fact, detailed analyses of toy models provide fundamental no-go results which state that the best *possible* decomposition takes the form of a diverging asymptotic series whose optimal truncation yields a separation between fast and slow degrees of freedom that is exponentially accurate as a function of a scale separation parameter such as the Rossby number (see MacKay, 2004; Vanneste, 2013, and references therein).

On the other hand, there are many reasons why the separation of a flow into its balanced and unbalanced components is desirable. The need for balanced initialization of numerical weather prediction models was recognized early (e.g. Lynch, 2006). Further, gravity waves play an important role in the dynamics of the atmosphere; unresolved gravity waves are thought of as a major source of uncertainty in numerical weather prediction and the atmospheric component of climate models (e.g. Alexander et al., 2010; Kim et al., 2003). The role of gravity waves for the energy budget of the ocean is less well understood, but potentially important (see von Storch et al., 2019, and references therein). To better understand the processes associated with gravity wave dynamics and to develop effective gravity wave parametrizations for numerical models where required, good diagnostic tools are important.

Available techniques for the separation of balanced and unbalanced flow range from time filtering, decomposition in terms of linear normal modes, nonlinear normal mode initialization (Baer and Tribbia, 1977; Machenhauer, 1977), and a variety of different asymptotic techniques (McIntyre, 2015; McIntyre and Roulstone, 2002; Oliver, 2006; Salmon, 1998; Warn et al., 1995). Viúdez and Dritschel (2004) introduced the concept of *optimal potential vorticity balance*, a modification of a Lagrangian contour-advecting numerical code in which the perturbation potential vorticity is slowly "ramped" from a trivial state to a fully nonlinear state "in which the amount of initia-gravity waves is minimal". Their approach, described in more detail in section 2, is attractive because it produces high quality balance without any explicit asymptotics at non-trivial, but moderate computational expense. Cotter (2013) realized that Viúdez and Dritschel's procedure can be understood theoretically in terms of adiabatic invariance of slow manifolds. He provided an argument showing, in the context of a toy model, that the resulting balance is exponentially accurate, just as balance itself can only be defined up to exponentially small remainders. Cotter's argument is based on performing the required integration over an infinite time horizon, while any practical implementation, of course, must be restricted to a finite time horizon. Gottwald et al. (2017) studied the same toy model on a finite time horizon. They realized that the required ramp function must satisfy consistency conditions at the temporal boundary points that preclude the use of analytic normal form theory for the analysis. Yet, they were able to prove exponential estimates, albeit with a smaller power of the time separation parameter in the exponent. Thus, the state produced by "optimal balance" (here *not* "optimal *potential vorticity* balance" because the principle goes beyond a potential vorticity formulation of the problem) is not optimal in the strict sense, but very good in the sense that the remainder is small beyond all orders, and arguably the best *practically accessible* algorithm for flow separation.

In this paper, we demonstrate that optimal balance for geophysical flow is not restricted to PV-based numerical codes as used by Viúdez and Dritschel (2004). Here, we take the simple situation of the single-layer rotating shallow water equations on the f-plane in primitive velocity-height variables and implement optimal balance on top of a pseudo-spectral model code. We explore several variations of the algorithm, in particular different choices of the "base-point coordinate" (the coordinate field left invariant by the procedure), different ramp functions, different ramp times, and different

choices of linear-end boundary conditions.

Our simulations demonstrate that the performance of optimal balance depends in an essential way on the choice of base-point coordinate and on the appropriate choice of the linear projector onto the slow linear subspace. We find that, even though the evolutionary model is formulated in primitive variables, potential vorticity based end-point conditions are advantageous. In particular, the only universally robust linear projector is the oblique projector onto the Rossby modes along the gravity wave modes which can be interpreted as the distinct non-orthogonal projector onto the Rossby modes that preserves the linear potential vorticity. Hence, the projector can be formulated as an elliptic partial differential equation which holds promise for using the method to produce an accurate nonlinear mode decomposition for more general models without the need to resort to asymptotic analysis.

The paper is organized as follows: Section 2 presents a brief review of optimal potential vorticity balance. In section 3, we describe the rotating shallow water equations in primitive variables, discuss scalings, describe the method of optimal balance in this setting, and discuss different options for the boundary conditions at the temporal end points. Section 4 introduces the experimental set-up including numerical implementation details and diagnostics. The simulation results and their behavior under changes of the experimental design are presented in section 5. The paper ends with a short general discussion and conclusions.

2. Optimal potential vorticity balance

Optimal potential vorticity balance as suggested by Viúdez and Dritschel (2004) is based on the formulation of the equations of motion in terms of the materially conserved potential vorticity (PV) q and two additional fields, the horizontal divergence δ and the ageostrophic horizontal vorticity γ. Both the rotating shallow water equations and various versions of the Euler–Boussinesq system in three dimensions can be cast into this general form

$$\partial_t q + \boldsymbol{u} \cdot \boldsymbol{\nabla} q = 0\,, \tag{1a}$$

$$\partial_t \begin{pmatrix} \delta \\ \gamma \end{pmatrix} = \frac{1}{\varepsilon}\,\mathcal{L} \begin{pmatrix} \delta \\ \gamma \end{pmatrix} + \mathcal{N}(q, \delta, \gamma)\,, \tag{1b}$$

where ε denotes the Rossby number, $\mathcal{L}$ is a linear operator with purely imaginary spectrum, and $\mathcal{N}$ contains all nonlinear terms which remain regular as $\varepsilon \to 0$ (e.g. Franzke et al., 2019; McIntyre and Norton, 2000; Mohebalhojeh and Dritschel, 2001; Vanneste, 2013). The system must be augmented by a PV inversion equation to recover the velocity $\boldsymbol{u}$ from (q, δ, γ). When the nonlinear interactions are switched off, (1) expresses an *exact* splitting between the slow variable q and the fast variables (δ, γ), so that the linear slow manifold is characterized by $\delta = \gamma = 0$.

The approach of Viúdez and Dritschel is based on a numerical approximation to the Lagrangian form of (1a),

$$q(\boldsymbol{\eta}_t(\boldsymbol{a}), t) = q_0(\boldsymbol{a})\,, \tag{2}$$

where $\boldsymbol{\eta}_t$ denotes the flow map satisfying $\partial_t \boldsymbol{\eta}_t(\boldsymbol{a}) = \boldsymbol{u}(\boldsymbol{\eta}_t(\boldsymbol{a}), t)$ and q_0 denotes the initial PV field. Observing that $\mathcal{N}(q_\mathrm{r}, \delta, \gamma) = 0$ for some background PV field q_r, non-zero in spherical geometry, they consider a modified evolution over a horizon of

artificial time $\tau \in [0, T]$ with associated flow map $\boldsymbol{\eta}_\tau$ where the materially advected PV is "ramped" up from the background state at $\tau = 0$ to a given PV field q^* at $\tau = T$. More precisely, they replace (2) by

$$q(\boldsymbol{\eta}_\tau(\boldsymbol{x}), \tau) = q_\mathrm{r}(\boldsymbol{\eta}_\tau(\boldsymbol{x})) + \rho(\tau/T)\,(q^*(\boldsymbol{x}) - q_\mathrm{r}(\boldsymbol{x}))\,, \tag{3}$$

where the ramp function ρ is a smooth function with $\rho(0) = 0$ and $\rho(T) = 1$, e.g. the cosine ramp

$$\rho(\theta) = (1 - \cos(\pi\theta))/2\,, \tag{4}$$

and impose the *final-time condition* $\boldsymbol{\eta}_T = \mathrm{id}$ which ensures, in particular, that $q(\boldsymbol{x}, T) = q^*(\boldsymbol{x})$.

The evolution of δ and γ in artificial time is governed by (1b) with τ in place of t and *initial condition*

$$\delta(\boldsymbol{x}, 0) = \gamma(\boldsymbol{x}, 0) = 0\,. \tag{5}$$

Finally, the PV inversion remains unaltered. The problem is thus turned into a boundary value problem in artificial time which is solved by a backward-forward nudging procedure, i.e., by integrating the system repeatedly backward and forward, imposing the respective initial or final-time condition after each half-iteration (e.g. Auroux and Nodet, 2012). This procedure is reported to converge quickly and robustly to a solution of the boundary value problem.

This scheme can be naturally implemented on top of the Contour-Advective Semi-Lagrangian (CASL) scheme (Dritschel and Ambaum, 1997; Dritschel et al., 1999) where the final-time condition is imposed by simply restoring all potential vorticity contours to the the contours defining q^* and where the ramp function acts on the values of the discrete set of vorticity levels. Viúdez and Dritschel (2004) tested the method for two systems, the three-dimensional non-hydrostatic Euler–Boussinesq system on the f-plane and the two-dimensional rotating shallow water equations on the sphere. In both cases, they report rapid convergence of the backward-forward nudging scheme to a solution whose ageostrophic variables $\delta(\boldsymbol{x}, T)$ and $\gamma(\boldsymbol{x}, T)$ are in excellent balance for the specified PV field $q^*(\boldsymbol{x})$.

However, most operational models are formulated in Eulerian primitive variables. It is *a priori* not clear if and how optimal balance can be used on top of such more common models. In the following, we show that this is indeed possible with comparable ease and robustness.

3. Optimal balance for the rotating shallow water equations

3.1. Semi-geostrophic and quasi-geostrophic scaling

The rotating shallow water equations describe the evolution of columns of shallow water of mean height H_0, free surface displacement $h = h(\boldsymbol{x}, t)$, and horizontal velocity field $\boldsymbol{u} = \boldsymbol{u}(\boldsymbol{x}, t)$ in a rotating frame of reference. They read

$$\partial_t \boldsymbol{u} + \boldsymbol{u} \cdot \boldsymbol{\nabla}\boldsymbol{u} + f\,\boldsymbol{u}^\perp + g\,\boldsymbol{\nabla} h = 0\,, \tag{6a}$$

$$\partial_t h + \boldsymbol{\nabla} \cdot (h\boldsymbol{u}) + H_0\,\boldsymbol{\nabla} \cdot \boldsymbol{u} = 0\,, \tag{6b}$$

where $\boldsymbol{u}^\perp = (-v, u)$, f is the Coriolis parameter, and g the constant of gravitational acceleration. We nondimensionalize the system in the usual way (e.g. Vallis, 2017). Using the same letters with the understanding that from here onward all quantities are non-dimensional, and assuming an advective time scale, we obtain

$$\varepsilon \left(\partial_t \boldsymbol{u} + \boldsymbol{u} \cdot \boldsymbol{\nabla} \boldsymbol{u}\right) + \boldsymbol{u}^\perp + \frac{\mathrm{Bu}}{\varepsilon\, h_0} \boldsymbol{\nabla} h = 0\,, \tag{7a}$$

$$\partial_t h + \boldsymbol{\nabla} \cdot (h\boldsymbol{u}) + h_0\, \boldsymbol{\nabla} \cdot \boldsymbol{u} = 0\,, \tag{7b}$$

where $h_0 = H_0/H$,

$$\varepsilon = \frac{U}{fL} \tag{8}$$

denotes the *Rossby number*, assumed to be small, and

$$\mathrm{Bu} = \frac{c^2}{f^2\, L^2} = \frac{gH_0}{f^2\, L^2} \tag{9}$$

the *Burger number*. As usual, we use U to denote the characteristic horizontal velocity, L the characteristic horizontal length scale, H the characteristic perturbation height, and $c = \sqrt{gH_0}$ the characteristic speed of gravity waves. We get a sensible leading-order balance between Coriolis force and pressure gradient force,

$$\boldsymbol{u}_G = \boldsymbol{\nabla}^\perp h\,, \tag{10}$$

for any scaling with $\mathrm{Bu} = \varepsilon\, h_0$ which we assume henceforth. Two special cases are commonly discussed: the *quasi-geostrophic* limit where $\mathrm{Bu} = 1$ so that $h_0 = \varepsilon^{-1}$ and the *semi-geostrophic* limit where $\mathrm{Bu} = \varepsilon$ so that $h_0 = 1$, i.e., height perturbations may be of the same order of magnitude than the mean height. We will test the performance of optimal balance in both of these scaling regimes.

3.2. Eulerian time scales

In both cases, the slow dynamics is described by a balance relation, a formal asymptotic series defining a kinematic dependence of $\boldsymbol{u}$ on h which provides consistent corrections to the leading order geostrophic balance, i.e.,

$$\boldsymbol{u} = \boldsymbol{u}_G + \mathrm{O}(\varepsilon) \tag{11}$$

where all right-hand terms depend on h only. The time evolution of the slow dynamics is then exclusively described by the scaled continuity equation. The characteristic time scale of this evolution depends on the limit taken: In the quasi-geostrophic limit, we find that

$$\partial_t h = -\boldsymbol{\nabla} \cdot (h\boldsymbol{u}) - \varepsilon^{-1}\, \boldsymbol{\nabla} \cdot \boldsymbol{u} = \mathrm{O}(\varepsilon) + \mathrm{O}(1) = \mathrm{O}(1)\,. \tag{12}$$

In the semi-geostrophic limit,

$$\partial_t h = -\boldsymbol{\nabla} \cdot (h\boldsymbol{u}) - \boldsymbol{\nabla} \cdot \boldsymbol{u} = \mathrm{O}(\varepsilon) + \mathrm{O}(\varepsilon) = \mathrm{O}(\varepsilon)\,. \tag{13}$$

Thus, to study the evolution of nearly balanced flow over constant fractions of the eddy-turnover time for different values of ε, we must scale the time interval of evolution by ε^{-1} in the semi-geostrophic regime (this is consistent with, e.g., the scaling study by Dritschel et al., 2017). In the quasi-geostrophic regime, the time interval of evolution remains independent of ε.

3.3. Optimal balance in primitive variables

The underlying principle of optimal balance is a slow deformation of the equations of motion from a linear system at artificial time $\tau = 0$ to the fully nonlinear system at artificial time $\tau = T$. For the linear system, the decomposition into fast and slow modes is exact and, in simple domain geometries, explicit. Over the time horizon $[0, T]$, the fast energy remains adiabatically invariant. Thus, if the fast energy is exactly zero at $\tau = 0$, which is a computationally accessible state, it will remain approximately zero up to $\tau = T$, even though an explicit characterization of the nonlinear fast energy is typically not feasible.

Viúdez and Dritschel (2004) turned off the nonlinear interactions implicitly by ramping down the PV anomaly toward $\tau = 0$. Here, following the approach analyzed in the context of toy models by Cotter (2013) and Gottwald et al. (2017), we ramp the nonlinear interactions explicitly, writing

$$\varepsilon \left(\partial_\tau \boldsymbol{u} + \rho(\tau/T)\, \boldsymbol{u} \cdot \boldsymbol{\nabla} \boldsymbol{u} \right) + \boldsymbol{u}^\perp + \boldsymbol{\nabla} h = 0 \,, \tag{14a}$$

$$\partial_\tau h + \rho(\tau/T)\, \boldsymbol{\nabla} \cdot (h \boldsymbol{u}) + h_0\, \boldsymbol{\nabla} \cdot \boldsymbol{u} = 0 \,. \tag{14b}$$

At the "linear end", we supply a boundary condition of the form

$$\mathbb{P}_{\mathrm{GW}}(\boldsymbol{u}, h)\big|_{\tau=0} = 0 \,, \tag{14c}$$

where $\mathbb{P}_{\mathrm{GW}}$ is a projector onto the imbalanced, or gravity wave, component of the linear flow, see section 3.5 for details. At the "nonlinear end", we fix a base-point coordinate to a specified value, imposing

$$q(T) = q^* \quad \text{or} \quad h(T) = h^* \,. \tag{14d}$$

In the following, we shall write q_T, h_T, etc. for short.

In general, a slow manifold is described by a mapping from a *base-point coordinate* into the full phase space. As discussed, neither the mapping nor the choice of base-point coordinate is unique; we only require that the manifold is approximately invariant and that the vector field on the manifold is predominantly slow (cf. MacKay, 2004). To ensure that such mapping is well-defined, at least for sufficiently small values for the scale separation parameter ε, it should map from a variable that is dominated by the geostrophic component of the flow; its dimensionality is fixed by the leading-order geostrophic balance (10). Thus, the two options in (14d) are natural candidates for the base-point variable. The use of h is suggested by the general structure of a balance relation sketched in (11). The potential vorticity q was already used by Viúdez and Dritschel (2004). Generally, any balance relation of the form (11) implies a formal, asymptotically consistent kinematic relationship between potential vorticity q and height field h; in some but not all cases, this can be made rigorous (e.g. Çalık et al., 2013). Due to this kinematic relationship, we would expect that both q and h

can be used as base point; our results suggest that, with some qualifications, this is indeed the case.

3.4. Ramp functions

Gottwald et al. (2017) proved that optimal balance, in a finite-dimensional setting, is $\mathrm{O}(\varepsilon^n)$ accurate only if $\rho^{(i)}(0) = \rho^{(i)}(1) = 0$ for $i = 1, \ldots, n$. It is exponentially accurate only if this condition is satisfied for all $n \geq 1$. In this case, the ramp function cannot be analytic, so that the balance error is strictly worse than the usual $\mathrm{O}(\exp(-c/\varepsilon))$ invariance error of the slow manifold itself. For certain quasi-analytic ramp functions, an exponential bound of the form $\mathrm{O}(\exp(-c/\varepsilon^{1/3}))$ was obtained. These results show, in particular, that a linear ramp is only $\mathrm{O}(\varepsilon)$-accurate and the cosine ramp (4) is accurate to $\mathrm{O}(\varepsilon^2)$.

Noting that a "one-sided ramp" function can always be symmetrized so that it satisfies the final condition $\rho(1) = 1$, we study, besides the cosine ramp, the family

$$\rho(\theta) = \frac{f(\theta)}{f(\theta) + f(1-\theta)} \tag{15}$$

where $f(\theta) = \exp(-1/\theta)$ for the exponential case and $f(\theta) = \theta^k$; here, explicitly, with $k = 1, 3$.

3.5. Linear wave separation

When $\tau = 0$, the physical-time evolution of (14) reduces to the linear rotating shallow water equations

$$\varepsilon\, \partial_t \boldsymbol{u} + \boldsymbol{u}^\perp + \boldsymbol{\nabla} h = 0\,, \tag{16a}$$

$$\partial_t h + h_0\, \boldsymbol{\nabla} \cdot \boldsymbol{u} = 0\,, \tag{16b}$$

where wave separation is known to be exact (e.g. Vallis, 2017): On the 2π-doubly-periodic domain, using the Fourier representation

$$\boldsymbol{u}(\boldsymbol{x}, t) = \sum_{\boldsymbol{k} \in \mathbb{Z}} \boldsymbol{u}_{\boldsymbol{k}}(t)\, \mathrm{e}^{\mathrm{i}\boldsymbol{k}\cdot\boldsymbol{x}}\,, \tag{17}$$

likewise for h, where $\boldsymbol{k} = (k, l)$ is the wave number vector, and setting $\boldsymbol{z}_{\boldsymbol{k}} = (\boldsymbol{u}_{\boldsymbol{k}}, h_{\boldsymbol{k}})$, we write (16) as

$$\partial_t \boldsymbol{z}_{\boldsymbol{k}} = \mathrm{i} A_{\boldsymbol{k}} \boldsymbol{z}_{\boldsymbol{k}} \quad \text{with} \quad A_{\boldsymbol{k}} = \begin{pmatrix} 0 & -\mathrm{i}/\varepsilon & -k/\varepsilon \\ \mathrm{i}/\varepsilon & 0 & -l/\varepsilon \\ -h_0\, k & -h_0\, l & 0 \end{pmatrix}. \tag{18}$$

For every $\boldsymbol{k}$, the eigenvectors of $A_{\boldsymbol{k}}$ split into one Rossby mode corresponding to eigenvalue $\omega^{\mathrm{RW}}_{\boldsymbol{k}} = 0$ and two gravity wave modes with eigenvalues $\omega^{\mathrm{GW}}_{\boldsymbol{k}} = \pm(\varepsilon\, h_0\, |\boldsymbol{k}|^2 + 1)/\varepsilon^2$. In other words, the Rossby modes are spanned by the family $\operatorname{Ker} A_{\boldsymbol{k}}$ and the gravity waves modes are spanned by the family $\operatorname{Range} A_{\boldsymbol{k}}$.

In general, we define $\mathbb{P}_{\mathrm{RW}}$ as the projector onto the space of all Rossby modes and set $\mathbb{P}_{\mathrm{GW}} = I - \mathbb{P}_{\mathrm{RW}}$. Noting that $\operatorname{Ker} A_{\boldsymbol{k}}$ and $\operatorname{Range} A_{\boldsymbol{k}}$ are not orthogonal, there is

no canonical way of defining these projectors. First, two options for defining spectral projections are discussed and compared. For each fixed $\boldsymbol{k}$, we consider the *oblique projector* onto $\operatorname{Ker} A_{\boldsymbol{k}}$ along $\operatorname{Range} A_{\boldsymbol{k}}$,

$$\mathbb{P}_{\boldsymbol{k}}^{\mathrm{RW,oblique}} = \frac{1}{h_0\,|\boldsymbol{k}|^2 + \varepsilon^{-1}} \begin{pmatrix} h_0\,l^2 & -h_0\,kl & -\mathrm{i}l/\varepsilon \\ -h_0\,kl & h_0\,k^2 & \mathrm{i}k/\varepsilon \\ \mathrm{i}h_0\,l & -\mathrm{i}h_0\,k & 1/\varepsilon \end{pmatrix} \tag{19}$$

vs. the *orthogonal projector* onto $\operatorname{Ker} A_{\boldsymbol{k}}$,

$$\mathbb{P}_{\boldsymbol{k}}^{\mathrm{RW,orth}} = \frac{1}{|\boldsymbol{k}|^2 + 1} \begin{pmatrix} l^2 & -kl & -\mathrm{i}l \\ -kl & k^2 & \mathrm{i}k \\ \mathrm{i}l & -\mathrm{i}k & 1 \end{pmatrix} . \tag{20}$$

We note that in the quasi-geostrophic scaling limit where $h_0 = \varepsilon^{-1}$, oblique and orthogonal projection coincide; in general, they differ, where the orthogonal projection is independent of the chosen scaling limit. The oblique projection never alters the energy contained in the Rossby modes, while the orthogonal projection will generally do so. When used in a backward-forward nudging scheme, this impacts convergence of the scheme even though the boundary condition (14c) is mathematically independent of the type of projection.

For more general models or more general domain geometries, a normal mode decomposition with associated explicit projection matrices may not be available, so that a PDE-based approach is desirable. Since geostrophic balance (10) is an *exact* characterization of the slow subspace spanned by the Rossby modes for the linearized system (16), we can also define the projector implicitly via (10). Again, this can be done in several ways.

The most naive approach is to leave h invariant and compute $\boldsymbol{u}$ from h via (10). However, within a backward-forward nudging scheme, this will lead to successive differentiation of the solution at the boundary, therefore to multiple "loss of derivatives" as the scheme is iterated, leading to amplification of small-scale noise and possibly loss of convergence of the scheme.

A second, more sophisticated approach is to start from $\boldsymbol{u}$, compute h by inverting

$$\Delta h = \zeta\,, \tag{21}$$

then recompute $\boldsymbol{u}$ via (10), effectively projecting $\boldsymbol{u}$ on its divergence-free component. This procedure avoids "losing derivatives". However, as we shall see in our experiments, this procedure is still not working well in all cases.

A third approach is motivated by the idea of defining a projection which fixes PV. At the linear end, the intrinsic quantity is *linear potential vorticity*,

$$q_{\mathrm{lin}} = \varepsilon\,\zeta + h/h_0\,. \tag{22}$$

This expression is obtained by linearizing the full shallow water PV and dropping additive and multiplicative constants as they will not affect the resulting computation. Linear PV is conserved by the linear shallow water equations (16) just as the usual potential vorticity is conserved by the full rotating shallow water equations.

We now impose the condition that the new state $(\boldsymbol{u}', h')$ at the linear end is in

geostrophic balance, i.e.,

$$\boldsymbol{u}' = \boldsymbol{\nabla}^{\perp} h' \tag{23}$$

subject to the constraint that linear PV is preserved. Thus, we must solve

$$-\varepsilon\, \Delta h' + h'/h_0 = q_{\text{lin}} \tag{24}$$

or, inserting (22) and solving for h',

$$h' = (h_0^{-1} - \varepsilon\, \Delta)^{-1} (\varepsilon\, \boldsymbol{\nabla}^{\perp} \cdot \boldsymbol{u} + h/h_0)\,. \tag{25}$$

All the operators on the right are linear constant-coefficient operators, so (25) and (23) are easily written in spectral representation, namely

$$\boldsymbol{z}'_{\boldsymbol{k}} = \frac{1}{h_0\, |\boldsymbol{k}|^2 + \varepsilon^{-1}} \begin{pmatrix} -\mathrm{i}l \\ \mathrm{i}k \\ 1 \end{pmatrix} \begin{pmatrix} \mathrm{i}l\, h_0 & -\mathrm{i}k\, h_0 & \varepsilon^{-1} \end{pmatrix} \boldsymbol{z}_{\boldsymbol{k}} \tag{26}$$

Observe that the matrix on the right hand side is *identical* to the oblique projector (19)! In other words, the oblique projector which arises through the elementary linear algebra of the spectral mode decomposition has an interpretation in terms of partial differential equations, equation (25), which does not depend on the availability of explicit normal modes. This correspondence comes about by imposing invariance of—perhaps not surprisingly—linear PV. Our results, detailed in section 5, strongly support the use of PV based approaches, not only for the linear-end but also for the nonlinear-end boundary condition. The use of nonlinear PV at the nonlinear end boundary requires some setup work, too, which we explain in the following.

3.6. Nonlinear-end boundary condition and PV inversion

In Section 5, we will compare the performance of h vs. q as base-point coordinate for optimal balance. When h is the base-point coordinate and the stopping criterion (see section 4.4) after a backward-forward integration cycle is not satisfied, we simply set $h_T := h^*$ and repeat.

When q is used as base-point coordinate, we will need to express $(\boldsymbol{u}, h)$ in terms of (q, δ, γ) kinematically. In this case, when the stopping criterion is not satisfied, we set $q_T := q^*$, keeping δ_T and γ_T unchanged, then recompute $(\boldsymbol{u}_T, h_T)$ and continue the nudging iteration. Thus, even when q is used as base-point coordinate, the evolution in (artificial) time will always be computed via the same pseudo-spectral code in $\boldsymbol{u}$-h variables.

To implement this procedure for the rotating shallow water equations (7), we recall that

$$q = \frac{\varepsilon\, \zeta + 1}{h_0 + h}\,, \qquad \delta = \boldsymbol{\nabla}^{\perp} \cdot \boldsymbol{u}\,, \qquad \gamma = \zeta - \Delta h\,, \tag{27}$$

with relative vorticity $\zeta = \boldsymbol{\nabla}^{\perp} \cdot \boldsymbol{u}$. These are the relations we need to invert. First, we

write out the Helmholtz decomposition

$$\boldsymbol{u} = \boldsymbol{\nabla}^{\perp}\psi + \boldsymbol{\nabla}\phi + \bar{\boldsymbol{u}} \tag{28}$$

with stream function ψ and velocity potential ϕ which are obtained by solving two Poisson equations, $\Delta\psi = \zeta$ and $\Delta\phi = \delta$, here with doubly-periodic boundary conditions. The mean velocity $\bar{\boldsymbol{u}}$ cannot be recovered from (q, δ, γ). In our specific case, $\bar{\boldsymbol{u}}$ is always known because the time evolution is computed in $\boldsymbol{u}$-h variables; in general, $\bar{\boldsymbol{u}}$ must be evolved alongside of (q, δ, γ) through evolving the average of the momentum equation (7a) over the fluid domain.

Second, to determine the height field h, we eliminate ζ from the definitions of q and γ in (27) and write the resulting expression in the form

$$(q - \varepsilon\Delta)h = \varepsilon\,\gamma - q\,h_0 + 1\,. \tag{29}$$

In our pseudo-spectral code, we split q into its mean $\bar{q}$ and mean-free components $q - \bar{q}$, keep the constant-coefficient part on the left, move the remainder expression to the right, and solve iteratively. This procedure converges quickly provided $\bar{q} > 0$ and $q - \bar{q}$ is sufficiently small.

4. Experimental set-up

4.1. Numerical implementation

We use a single numerical code which can solve the rotating shallow water equations in physical time or, with ramp function present, in artificial time. The code can be used either forward in time, as an initial value problem, or backward in time, as a final value problem. Thus, when solving the optimal balance boundary value problem (14), we can use the following backward-forward nudging procedure. Starting at the final time $\tau = T$, from a given state $(\boldsymbol{u}^*, h^*)$, we integrate *backward* to artificial time $\tau = 0$, where we impose the linear-end boundary condition (14c). We then integrate *forward* to artificial time $\tau = T$ where we impose one of the nonlinear-end boundary conditions (14d). This cycle is repeated until convergence is reached, see section 4.4 for a detailed discussion. The balanced state is then given by the values of $\boldsymbol{u}(T)$ and $h(T)$, or $(\boldsymbol{u}_T, h_T)$ for short. When solving the rotating shallow water equations (7) in physical time, the ramp function is inactive and we run the code in the usual way.

The 2π-doubly-periodic domain is discretized by $n = 256$ equidistant grid points in each spatial direction. Our code is a modification of the open source code PyRsw by Poulin (2016). Derivatives are computed spectrally, products in physical space with full dealiasing so that the effective maximal wave-number is $n/3$. Time stepping is done with the third-order Adams–Bashforth method where the time step is given by $\Delta t = n_{\text{cfl}}\,\Delta x/(\max|\boldsymbol{u}| + 2\,\varepsilon^{-1})$ with CFL number $n_{\text{cfl}} = 0.5$. We verified that the results presented here are not sensitive to the details of the time stepper and time step selection.

As the ramp-time and also the physical-time evolution used to compute the "diagnosed imbalance"—see section 4.3 below—is on the order of one eddy turnover period or less, dissipation is not important so that most of the runs where done with viscosity switched off. However, we did perform tests with a viscosity of the form $\varepsilon/\mathrm{Re}\,\Delta\boldsymbol{u}$ with

Reynolds number

$$\mathrm{Re} = \frac{UL}{\nu} \tag{30}$$

where ν is the kinematic viscosity. When used in the optimal balance problem, the viscous term is multiplied by the ramp function as well. This choice reflects the fact that when the nonlinearity is ramped down, possible transfer of energy to small scales is also inhibited so that eddy viscosity in the sense of a dissipative turbulence closure is not necessary. Viscosity is always acting dissipatively in the direction of integration to ensure stability of the model. Thus, when integrating backward, the sign of the dissipative term is reversed.

4.2. Initial conditions

Our experiments start from a random height field h with spectral "energy" at wave number $k = |\boldsymbol{k}|$ given by $\mathcal{E} = k^{3/2}/(k + a\,k_0^2)^b$ where $a = (2b-3)/3$ and $b = (7+d)/4$. The parameters k_0 and d control the location of the spectral maximum and the asymptotic rate of decay, respectively. We choose $k_0 = 6$ and $d = 6$ throughout. The randomly generated perturbation height h is taken to be mean free and normalized such that $|h| < 0.2$; the mean height satisfies $h_0 = 1$ for the semi-geostrophic scaling tests and $h_0 = \varepsilon^{-1}$ for the quasi-geostrophic case.

For the corresponding velocity field $\boldsymbol{u}$, we use two choices. Setting $\boldsymbol{u} = \boldsymbol{u}_G$ creates a condition which is balanced to leading order. Most of our tests are done in this configuration. In addition, we test a strongly imbalanced situation where h is chosen as described above, but we set $\boldsymbol{u} = 0$. We note that when h is the base-point coordinate for optimal balance, these two choices must produce the same balanced state and may only differ in their convergence behavior. When q is used as the base-point coordinate, these two choices will generally lead to different balanced states.

4.3. Diagnosed imbalance

Since the "true" optimally balanced state is not practically available, we must define a computationally accessible proxy to assess the quality of balance obtained. As in Gottwald et al. (2017), we use the *diagnosed imbalance* defined as follows.

(i) Balance the initial configuration $(\boldsymbol{u}^*, h^*)$ via solving the optimal balance boundary value problem (14) over ramp time T to obtain the balanced flow $(\boldsymbol{u}_T, h_T)$.
(ii) Evolve $(\boldsymbol{u}_T, h_T)$ up to physical time t' through the shallow water model (7); the final state is denoted $(\boldsymbol{u}', h')$.
(iii) Rebalance the state $(\boldsymbol{u}', h')$ via optimal balance, i.e, find a new balanced state $(\boldsymbol{u}'_T, h'_T)$.
(iv) Define the diagnosed imbalance as the relative difference between the imbalance variables of the evolved state (δ', γ') and and those of its rebalanced version, (δ'_T, γ'_T), setting

$$I = \frac{\|(\delta', \gamma') - (\delta'_T, \gamma'_T)\|}{\frac{1}{2}\left(\|(\delta', \gamma')\| + \|(\delta'_T, \gamma'_T)\|\right)}\,. \tag{31}$$

If optimal balance in step (i) provides a well-balanced flow, the evolution of $(\boldsymbol{u}_T, h_T)$ up

to physical time t' in step (ii) should stay close to the (approximate) balance manifold. Thus, the rebalancing step (iii) should not alter the evolved state by much. It is in this sense that the diagnosed imbalance provides a good computational proxy for the quality of balance.

4.4. Stopping criterion

The iterative nudging procedure for solving the temporal boundary value problem can be terminated in two ways. For the sake of exposition, let us suppose that q is the chosen base-point coordinate. When the relative difference between q_T and the prescribed base point q^* is below a small prescribed tolerance, we can definitely exit the loop. However, it turns out that for some combinations of linear-end and nonlinear-end boundary condition, the speed of convergence slows down to practically zero. In particular, when using base-point coordinate h, the scheme converges only up to a small persistent residual—see section 5.2. This leads us to choose a criterion which terminates the loop reliably for all but the diverging cases: we terminate the loop when

$$\frac{\|q_T(n+1) - q_T(n)\|}{\frac{1}{2}\left(\|q_T(n+1)\| + \|q_T(n)\|\right)} \leq \kappa\,, \tag{32}$$

where $q_T(n)$ and $q_T(n+1)$ denote successive iterates of the nudging iteration, with threshold $\kappa = 10^{-4}$. When h is used as base-point coordinate, everything described above is performed with h in place of q.

The threshold $\kappa = 10^{-4}$ works well across most of the simulations shown. When using q as base-point coordinate, a much smaller tolerance can be used, but will not improve the results shown. When using h as base-point coordinates and $\varepsilon \approx 1$, we need to choose $\kappa = 10^{-2}$ to be able to terminate the loop. In this case, the overall diagnosed imbalance is relatively large so that, again, the precise value of κ does not affect the results. It is important to note that the quality of balance is not affected by the choice of κ in condition (32). The quality of reaching the prescribed base point, on the other hand, depends on the details of the stopping criterion.

5. Results

Based on the outcome of preliminary exploration, we choose our base scheme as follows: potential vorticity q is used as base-point coordinate, the oblique projection (i.e., preservation of linear PV) is used for the linear-end boundary condition, and the exponential ramp function, i.e., (15) with $f(\theta) = \exp(-1/\theta)$ is used. These choices are assumed unless otherwise stated. In the following, we test variations of these choices as well as the effect of different ramp times T and forward integration times t'.

5.1. Qualitative assessment

We begin by presenting a visual demonstration of using optimal balance on a shallow water flow near balance and a second shallow water flow far from balance. The initial condition is selected as described in section 4.2, for both cases. The Rossby number is $\varepsilon = 0.1$ in semi-geostrophic scaling and the viscosity is zero. Starting from the random initial fields (figures 1 and 2, left column), the flow is first evolved in physical time up to

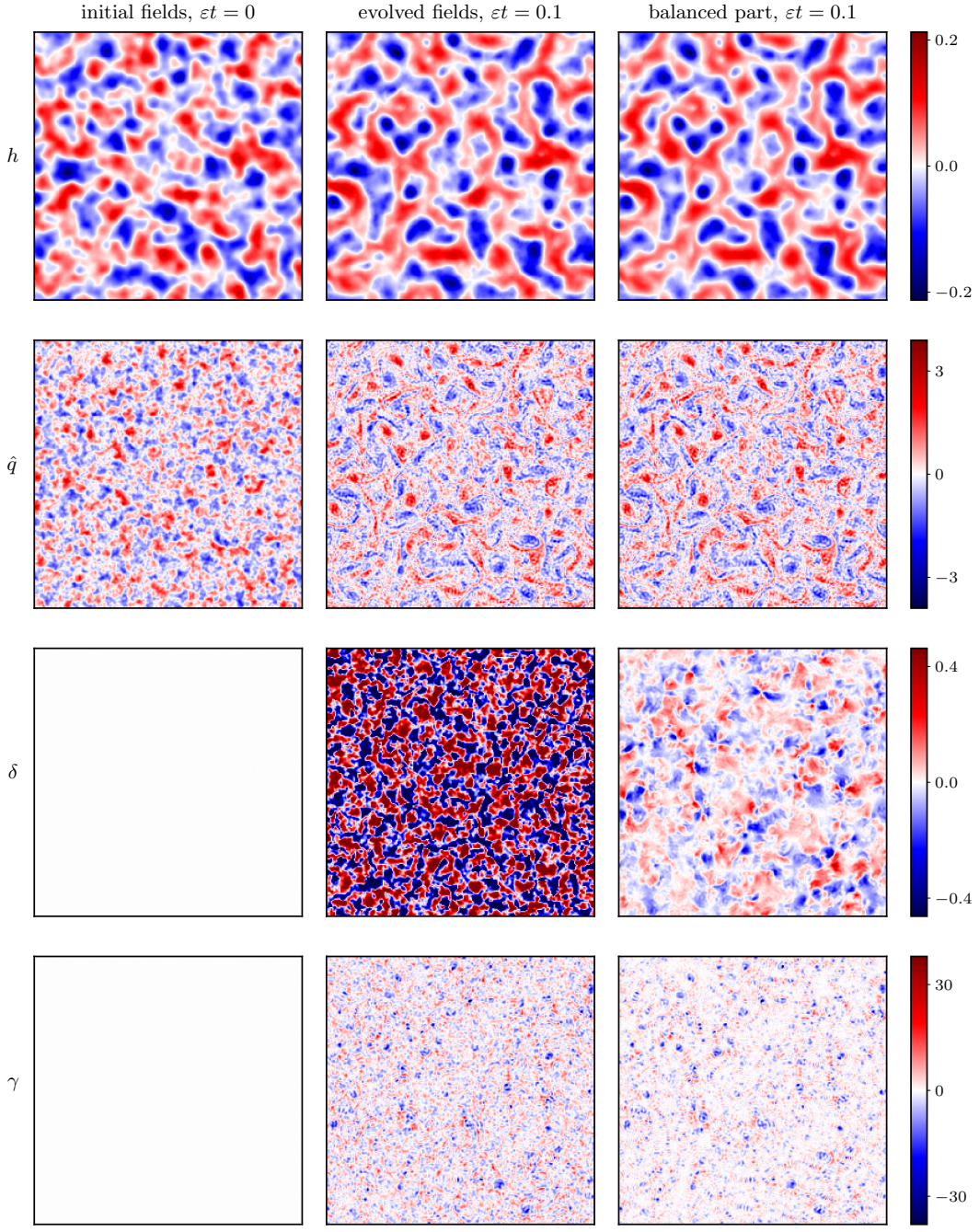

Figure 1. Shallow water free surface h (first row), mean-free potential vorticity $\hat{q} = q - \bar{q}$ (second row), divergence δ (third row) and ageostrophic vorticity γ (last row) in semi-geostrophic scaling. We display the initial fields in geostrophic balance (left column), evolved fields at $\varepsilon t = 0.1$ (middle column), and the balanced part of the evolved fields via optimal balance with base point q and ramp time $T = 0.1/\varepsilon$.

$t = 0.1/\varepsilon$ to create a more typical flow field (id., middle column), then balanced using optimal balance (id., right column). In the highly imbalanced test case, the evolution in physical time creates shock waves, i.e., small scale structures, visible especially in the δ and γ fields. Yet, optimal balance is able to extract the relatively smooth, and

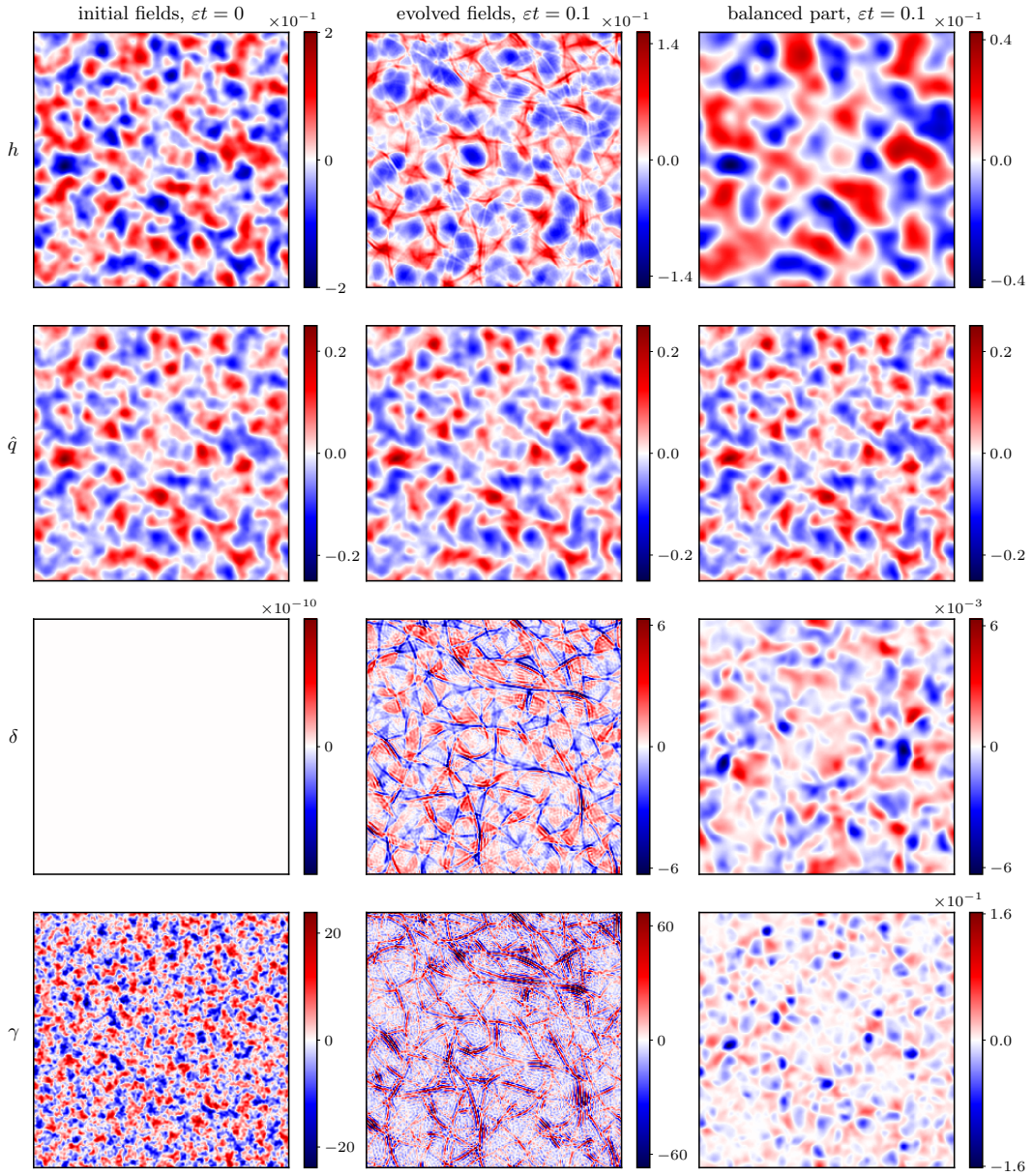

Figure 2. The same test case as in figure 1, except that the initial velocity is $\boldsymbol{u} = 0$ resulting in a strongly imbalanced flow.

much smaller balanced component of the flow. The use of q as base-point coordinate is clearly visible: the potential vorticity anomaly $\hat{q} = q - \bar{q}$ does not change during balancing. We remark that, due to the highly irregular h field in the second case, it is not possible to obtain a convergent optimal balance iteration with h as base point.

5.2. Convergence

In this section, we examine the convergence of the backward-forward nudging procedure for the different choices of boundary condition. We visualize convergence by plotting the Fourier spectra of a sequence of iterates at artificial time $\tau = T$ without

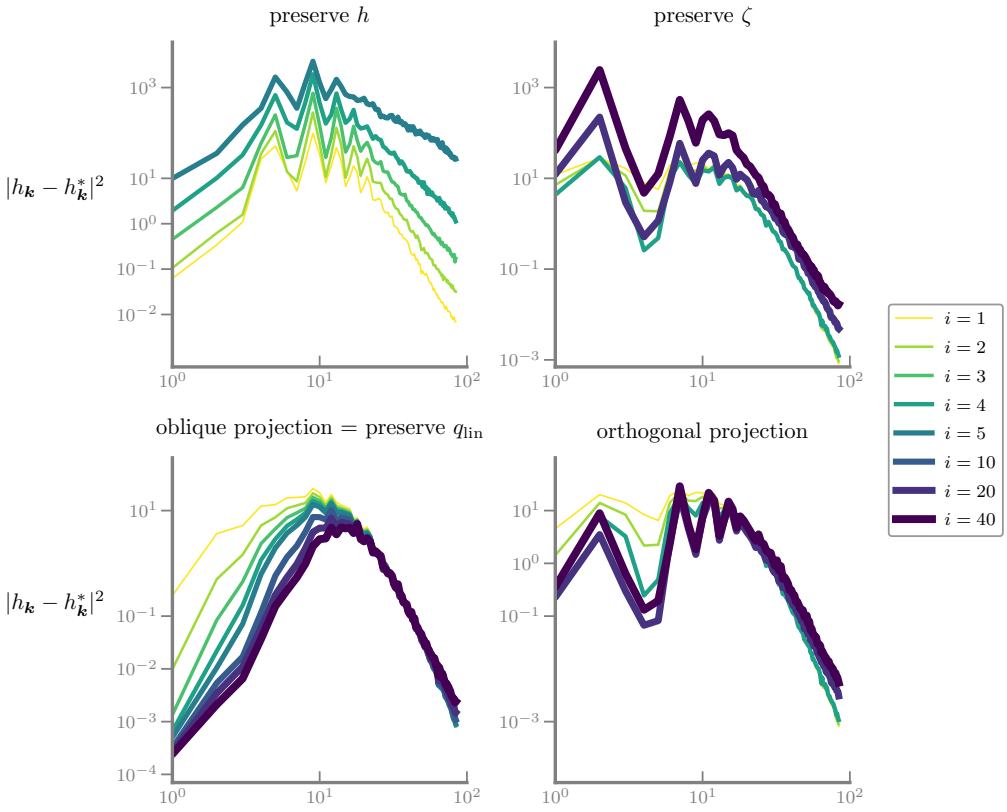

Figure 3. Energy spectra of selected nudging iterations with base point h for different linear-end boundary conditions. When h is preserved (top left), the scheme diverges rapidly and only the first five iterates are shown.

applying any stopping criterion. We present results for semi-geostrophic scaling with ramp time $\varepsilon T = 0.1$ and Rossby number $\varepsilon = 0.1$; results for the quasi-geostrophic case and for other values of ε are qualitatively similar.

First, preserving h at the linear end and using h as base-point coordinate at the nonlinear end leads to outright divergence, most strongly at the high wavenumbers (figure 3, top right). This is expected because of the loss of derivatives at the linear end without recovery at the nonlinear end. As we shall see below, when using q as base point, the nonlinear PV inversion is regularizing enough that preserving h at the linear end results in a converging nudging scheme. However, the parameter range of convergence is not as large as for other choices and convergence is slower, so that we can reject the h-preserving projection for the linear-end boundary condition outright.

Figure 3 also shows the three other linear projectors in combination with using h as base-point coordinate at the nonlinear end. Only the oblique projector yields a scheme that converges robustly for $\varepsilon = 0.1$. Divergence of the orthogonal projection and the ζ-preserving projection is more subtle, originating primarily on the large scales. We note that it is the large scales where the subspaces of Rossby and gravity wave modes are very non-orthogonal, so that any non-oblique projector will inject energy into the Rossby modes, possibly destabilizing the iteration on the large scales.

When taking q as base-point coordinate, all linear projectors yield a converging scheme, albeit of different quality. The scheme with oblique and orthogonal projector is converging well (figure 4, bottom row) while the h-preserving projector is slowing

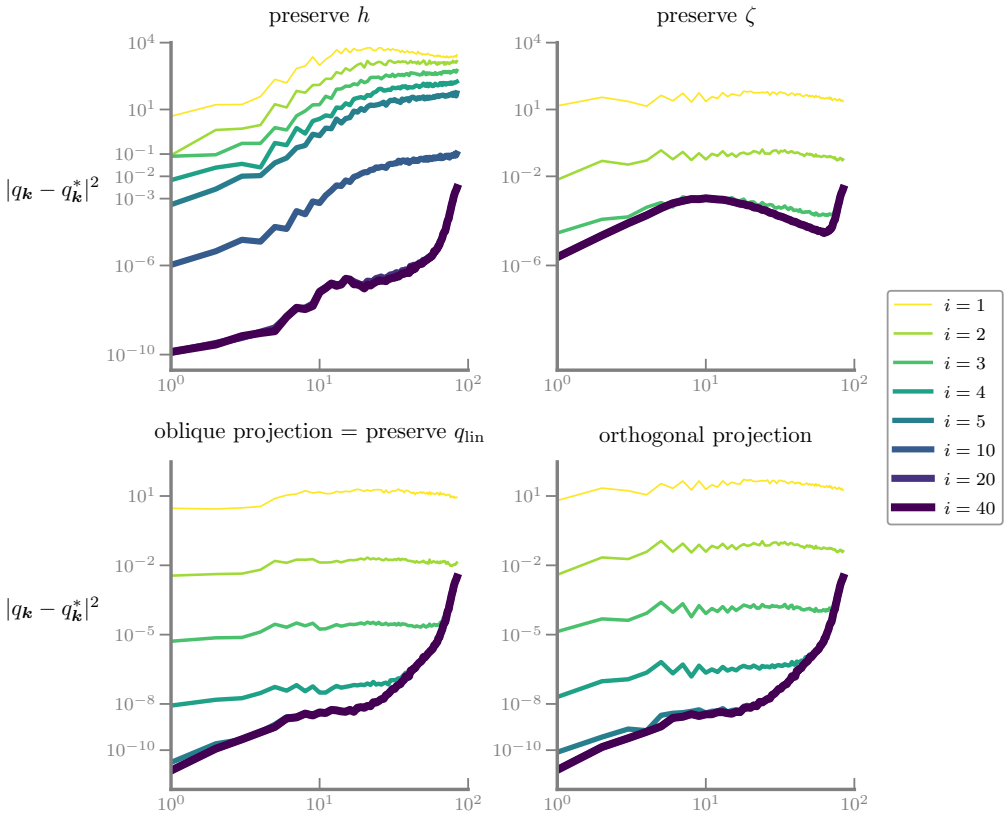

Figure 4. The same test case as figure 3, but using q as base-point coordinates with results for all four different linear-end conditions.

down convergence (id., top left) and the ζ-preserving projector is converging only up to a relatively large residual in the mid-range of scales (id., top right).

These result single out the oblique projector, which is q_{lin}-preserving, as the universally most robust choice for the linear-end condition. Since it can be formulated as a PDE, see (25), it can potentially be used for more complicated geometries and more complicated models as well. All further results shown below will use the oblique projector.

5.3. Optimal integration time scales

We now look at good choices for the ramp time T and the forward integration time t' in the definition of diagnosed imbalance. Figure 5 shows the diagnosed imbalance for the different fields across a range of ramp times and forward integration times t'. We see that the diagnosed imbalance is not very sensitive to the choice of forward integration time, but the sensitivity of the diagnostics decreases for longer forward integration times. Based on the results, we choose $t' = 0.5$ for the scaling analysis that follows. We further see that optimal balance has an optimal ramp time T. For quasi-geostrophic scaling (shown), good ramp times are $T = 0.5, \ldots, 2$, for semi-geostrophic scaling (not shown), good ramp times are $\varepsilon T = 0.05, \ldots, 0.2$ with $t' = 0.05$.

Figures 6 and 7 provide a detailed view of the scaling of diagnosed imbalance across a range of Rossby numbers for different ramp times, for quasi-geostrophic and semi-

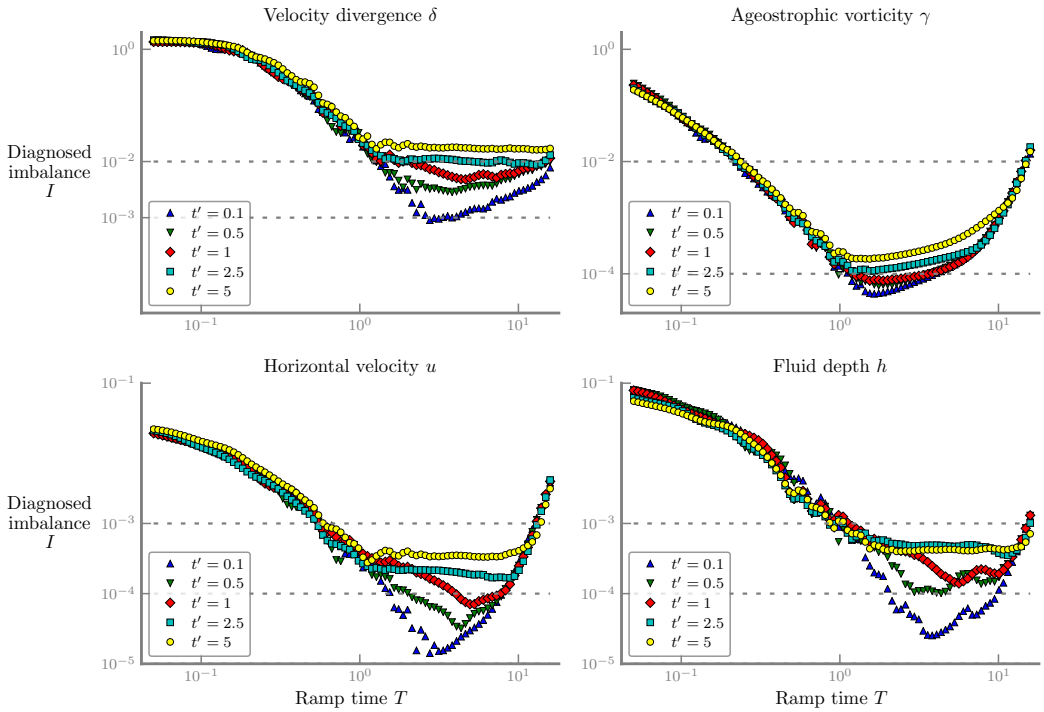

Figure 5. Diagnosed imbalance as a function of ramp time T in quasi-geostrophic scaling for different physical times t'. The base-point coordinate is q and we use the oblique projection, the exponential ramp function, and $\varepsilon = 0.1$.

geostrophic scaling, respectively. It is clearly seen that the advantage of longer ramp times persists across the entire range of Rossby numbers, except for saturation effects that are likely due to numerical limitations for very small values of ε. The scaling of diagnosed imbalance with ε, however, is not affected by the ramp time as predicted by the theory of Gottwald et al. (2017).

We stress that none of these results depend on the choice of the linear end boundary condition except when the algorithm does not converge. This occurs, notably, for the orthogonal projection in semi-geostrophic scaling for very small values of ε, a situation where the angle between fast and slow subspaces for small wave-numbers is very small.

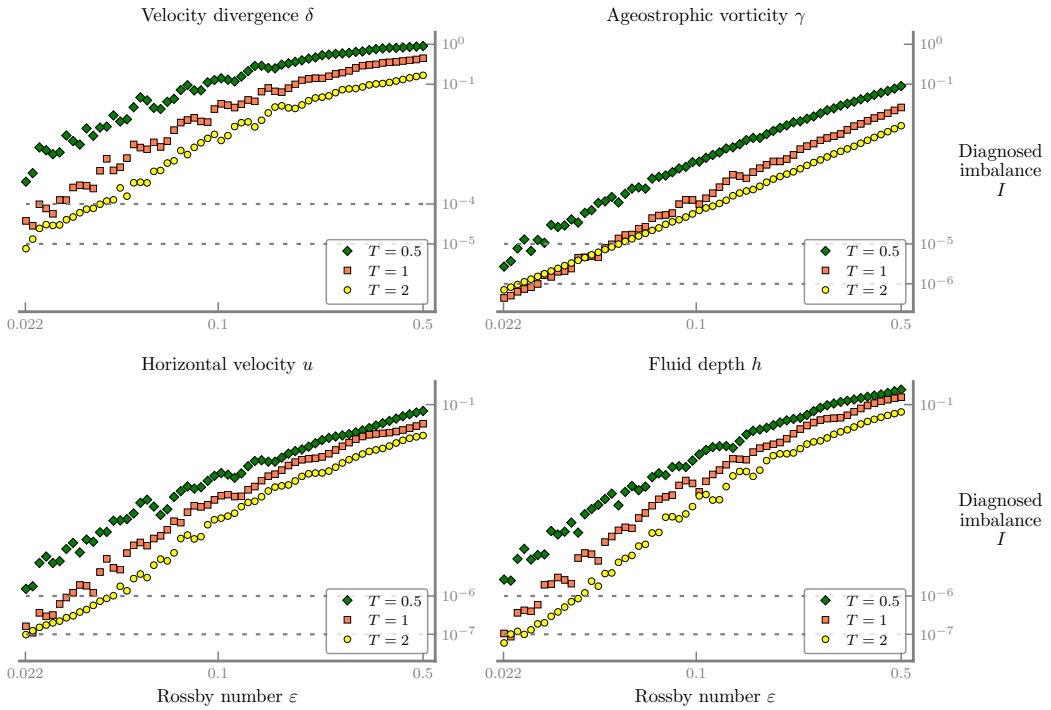

Figure 6. Diagnosed imbalance as a function of ε in quasi-geostrophic scaling for different ramp times T. The base-point coordinate is q, the exponential ramp function is used, and $t' = 0.5$.

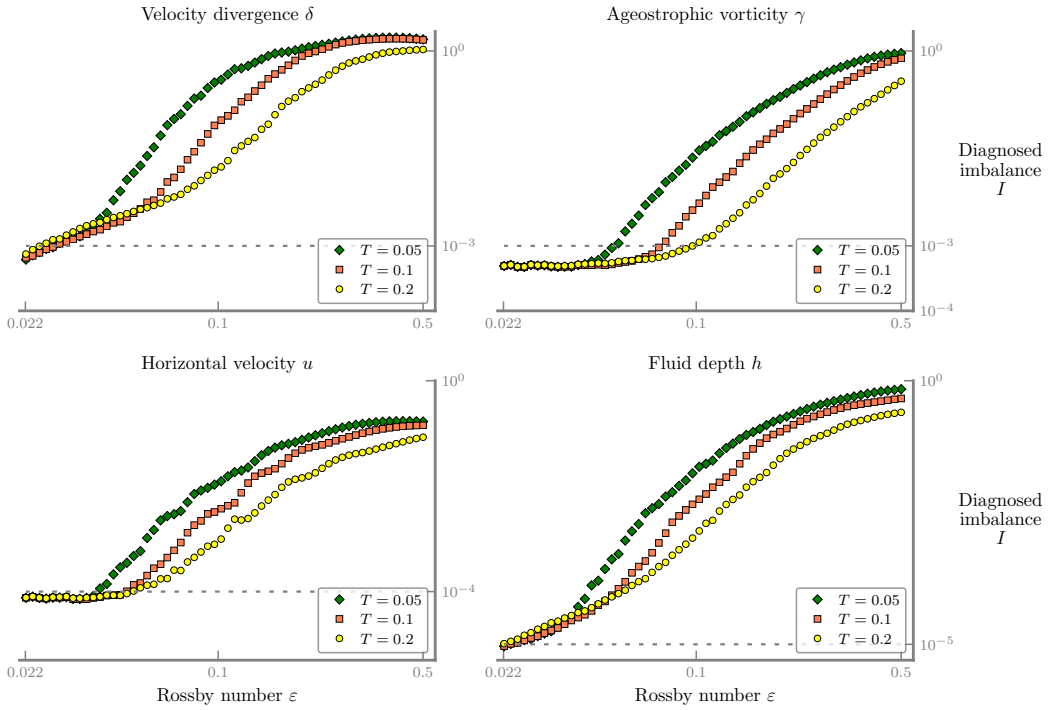

Figure 7. The same test as in figure 6 for semi-geostrophic scaling and $\varepsilon t' = 0.05$.

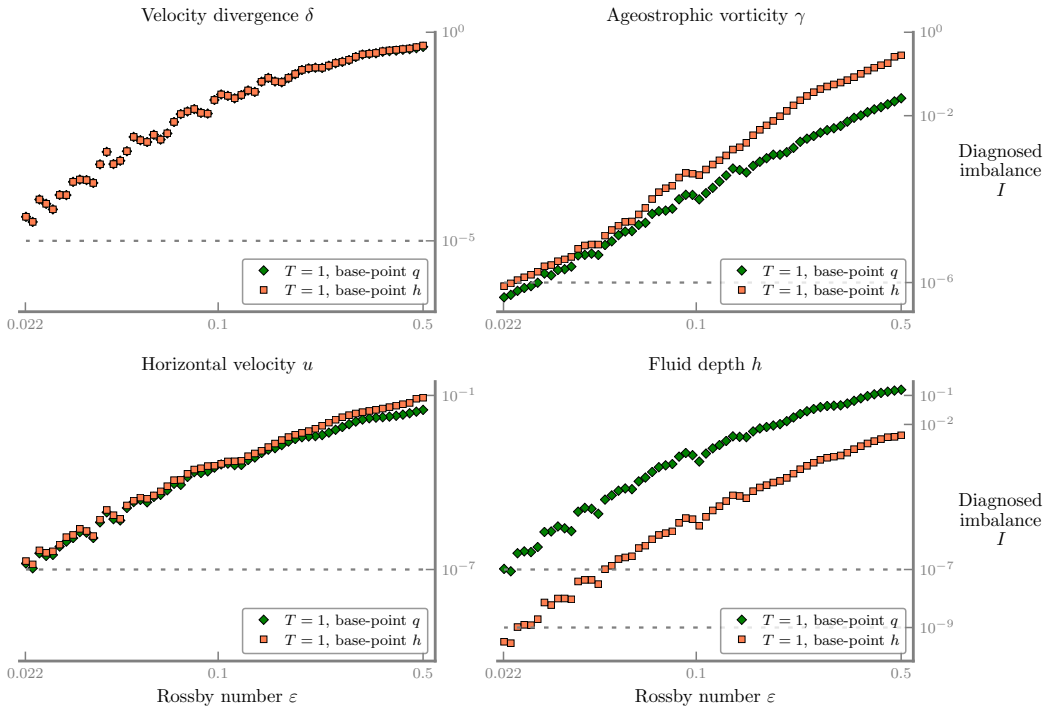

Figure 8. Diagnosed imbalance as a function of ε in quasi-geostrophic scaling for different base-points with $T = 1$ and $t' = 0.5$.

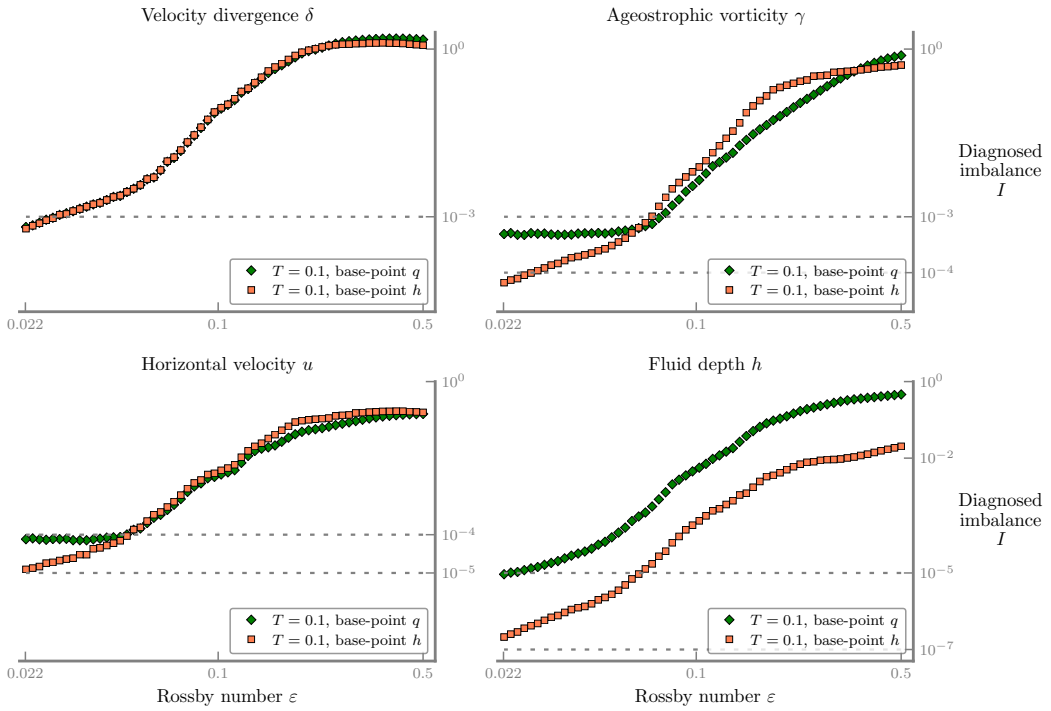

Figure 9. Same as figure 8 for semi-geostrophic scaling with $\varepsilon T = 0.1$ and $\varepsilon t' = 0.05$.

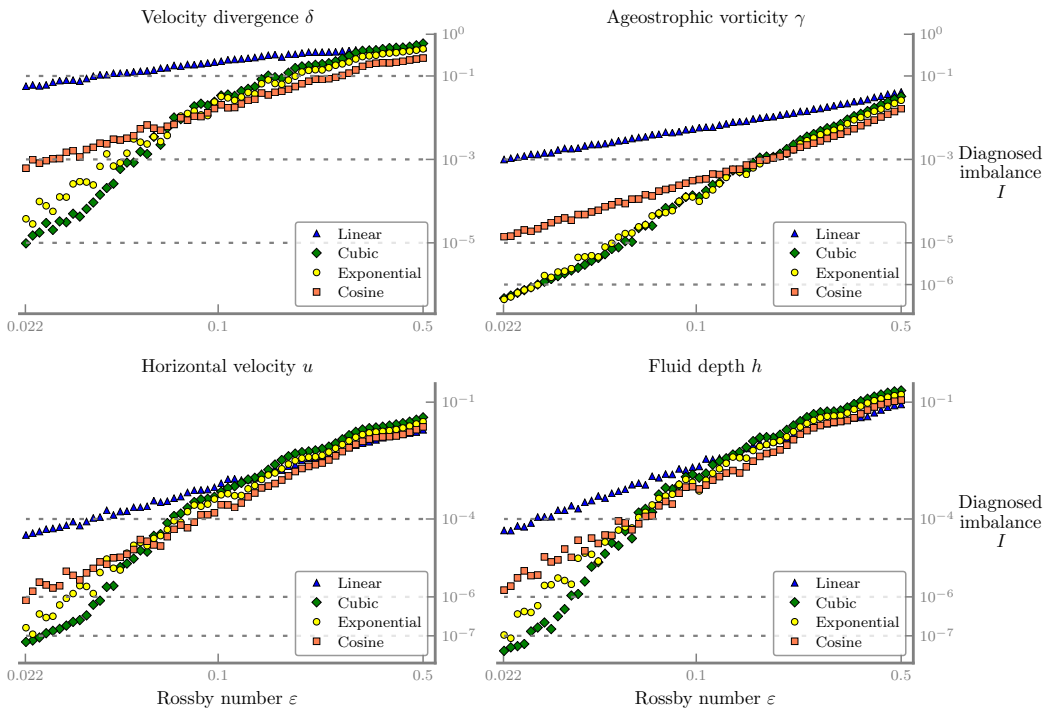

Figure 10. Diagnosed imbalance for different ramp functions in quasi-geostrophic scaling with base point q, $T = 1$, and $t' = 0.5$.

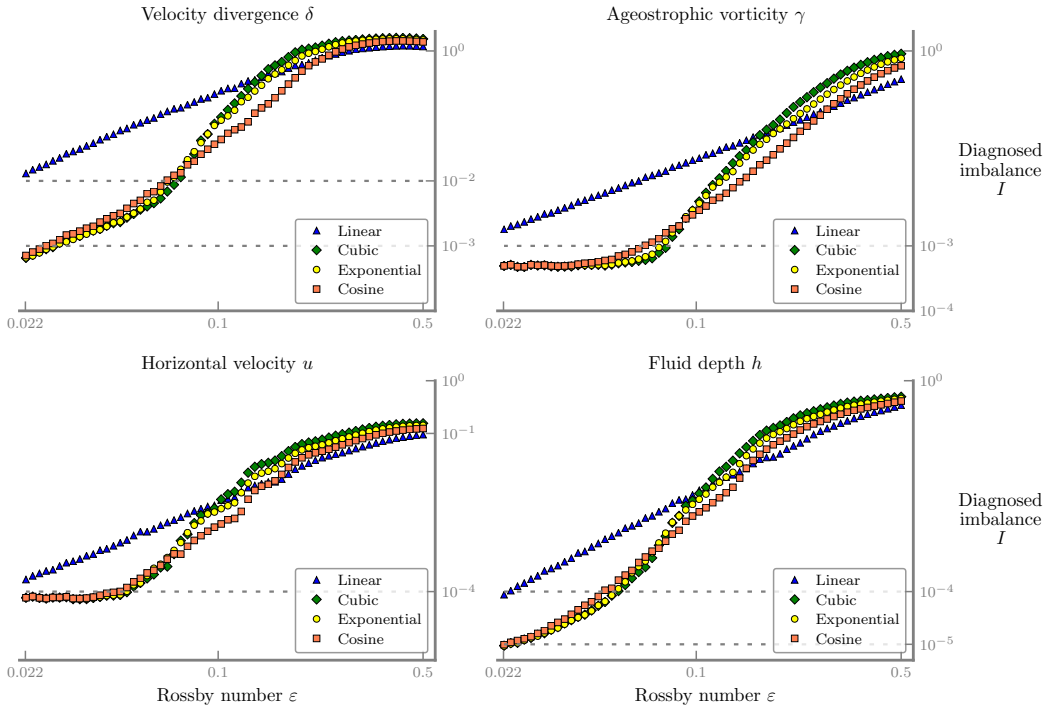

Figure 11. Same as figure 10 for semi-geostrophic scaling, $\varepsilon T = 0.1$, and $\varepsilon t' = 0.05$.

5.4. Choice of base-point coordinates

Figures 8 and 9 compare the two different choices of the base-point coordinate for quasi-geostrophic and semi-geostrophic scaling, respectively. The quality of balance is comparable, with a slight advantage for using q as base point for larger values of ε. When h is used as base point, even with the best-case oblique projector at the linear end, convergence takes place only up to a small persistent residual, cf. figure 3, bottom left. Thus, the diagnosed imbalance in h (figures 8 and 9, bottom right) is not exactly zero but still two orders of magnitude smaller than for the other fields.

These results suggest that, while it is well possible to use h as base-point coordinate, more robust and slightly better results are obtained by using q as base point. In particular, with q as base point, we can use much much smaller tolerance thresholds in the stopping criterion for the nudging iteration.

5.5. Choice of ramp function

Figures 10 and 11 compare different ramp functions for quasi-geostrophic and semi-geostrophic scaling, respectively. Three of the four choices are based on the ramp function (15) with $f(\theta) = \theta$ ("linear"), $f(\theta) = \theta^3$ ("cubic"), $f(\theta) = \exp(-1/\theta)$ ("exponential"); we also include the "cosine" ramp function (4) which is of second order.

Asymptotically, the higher order ramp functions do better, as expected, but the cut-over occurs relatively close to the point where other errors, likely due to the limited spatial resolution, dominate and limit the accuracy of optimal balance. The cosine ramp does best over large ranges of the practically interesting scaling regime, especially for the semi-geostrophic case, somewhat less so for quasi-geostrophic scaling. The reason is that that the balancing error not only depends on the compatibility conditions at the endpoints, but also on time derivatives of the ramp function. Since successive derivative of the cosine function are well-bounded, these error components tend to be small, in particular smaller than for the higher-order ramp functions which necessarily must be steeper in the center part of the ramp.

5.6. Viscosity

We investigated the performance of optimal balance with a coefficient of viscosity tuned to the value $\mathrm{Re} = 5 \times 10^3$ that is just large enough to avoid build-up of spectral energy near the resolution scale in a longer-time simulation. When used in the context of the optimal balance tests, the main effect is a reduction of small-scale energy in all evolved fields, with only minor impact on larger scales and on the balance diagnostics presented. We therefore conjecture that optimal balance can well be implemented on top of models where some form of explicit or implicit dissipation is necessary for numerical stability.

6. Discussion and Conclusion

We have shown, in the simple context of the f-plane rotating shallow water equations, that optimal balance can be implemented on top of existing primitive-variable numerical codes. It can yield good-quality balance, limited primarily by the accuracy of the numerical code. In the best case, residuals in the iterative solver are restricted to high modes near the spatial grid scale of the model. Thus, smoother flows can be balanced

with smaller residuals than rougher flows. For large parameter ranges, the cosine ramp function already used by Viúdez and Dritschel (2004) is a good compromise between order and pre-asymptotic accuracy, in some cases higher-order ramp functions can yield slight improvements.

Optimal balance crucially depends on two choice: the base-point coordinate which is kept fixed while the algorithm yields values for the remaining phase space variables, and the linear projector onto the slow (Rossby) modes at the linear end of the ramp. Using the oblique projector along the gravity modes onto the Rossby modes is universally the best choice. Interestingly, the oblique projector can be interpreted as the projector onto the Rossby modes which keeps linear potential vorticity invariant. It can be expressed via a linear PV-inversion relation as a PDE, so is expected to generalize readily to more complex models. This is yet another vindication of the beneficial role of PV-based numerics in geophysical fluid dynamics, here even in the situation where the evolutionary part of the code is intentionally not PV-aware. For the base-point coordinate, using PV has advantages, but using other coordinates, here in particular the height field, is well within the capability of the method.

We have not investigated performance on the equatorial β-plane or on the sphere. We conjecture that the robustness brought about by PV-based boundary condition will be even more pronounced in these cases where scale separation breaks down. Further, yet unexplored possibilities lie in using optimal balance on full atmosphere or ocean models. We do not expect fundamental obstacles, but the numerical treatment of the linear and non-linear end boundary conditions will require careful attention.

Acknowledgments

We thank Gualtiero Badin, Manita Chouksey, Colin Cotter, Sergey Danilov, David Dritschel, Carsten Eden, Georg Gottwald, Haidar Mohamad, Francis Poulin, Jacques Vanneste, and Jin-Song von Storch for interesting discussions on balance and optimal balance. This work contributes to the project "The Interior Energy Pathway" of the Collaborative Research Center TRR 181 "Energy Transfers in Atmosphere and Ocean" funded by the Deutsche Forschungsgemeinschaft (DFG, German Research Foundation) under project number 274762653.

References

Alexander, M. J., Geller, M., McLandress, C., Polavarapu, S., Preusse, P., Sassi, F., Sato, K., Eckermann, S., Ern, M., Hertzog, A., Kawatani, Y., Pulido, M., Shaw, T. A., Sigmond, M., Vincent, R., and Watanabe, S. (2010). Recent developments in gravity-wave effects in climate models and the global distribution of gravity-wave momentum flux from observations and models. *Q. J. R. Meteorol. Soc.*, 136:1103–1124.

Auroux, D. and Nodet, M. (2012). The back and forth nudging algorithm for data assimilation problems: theoretical results on transport equations. *ESAIM Control Optim. Calc. Var.*, 18(2):318–342.

Baer, F. and Tribbia, J. (1977). On complete filtering of gravity modes through nonlinear initialization. *Mon. Wea. Rev.*, 105:1536–1539.

Çalık, M., Oliver, M., and Vasylkevych, S. (2013). Global well-posedness for the generalized large-scale semigeostrophic equations. *Arch. Ration. Mech. Anal.*, 207(3):969–990.

Cotter, C. (2013). Data assimilation on the exponentially accurate slow manifold. *Phil. Trans. R. Soc. A*, 371(1991):20120300.

Dritschel, D. G. and Ambaum, M. H. (1997). A contour-advective semi-Lagrangian numerical algorithm for simulating fine-scale conservative dynamical fields. *Q. J. Roy. Meteor. Soc.*, 123(540):1097–1130.

Dritschel, D. G., Gottwald, G. A., and Oliver, M. (2017). Comparison of variational balance models for the rotating shallow water equations. *J. Fluid Mech.*, 822:689–716.

Dritschel, D. G., Polvani, L. M., and Mohebalhojeh, A. R. (1999). The contour-advective semi-Lagrangian algorithm for the shallow water equations. *Mon. Weather Rev.*, 127(7):1551–1565.

Franzke, C. L. E., Oliver, M., Rademacher, J. D. M., and Badin, G. (2019). Multi-scale methods for geophysical flows. In Eden, C. and Iske, A., editors, *Energy Transfers in Atmosphere and Ocean*, pages 1–51. Springer, Cham.

Gottwald, G. A., Mohamad, H., and Oliver, M. (2017). Optimal balance via adiabatic invariance of approximate slow manifolds. *Multiscale Model. Simul.*, 15(4):1404–1422.

Kim, Y., Eckermann, S. D., and Chun, H. (2003). An overview of the past, present and future of gravity-wave drag parametrization for numerical climate and weather prediction models. *Atmos. Ocean*, 41(1):65–98.

Lynch, P. (2006). *The Emergence of Numerical Weather Prediction: Richardson's Dream.* Cambridge University Press.

Machenhauer, B. (1977). On the dynamics of gravity oscillations in a shallow water model, with applications to normal mode initialization. *Beitr. Phys. Atmos.*, 50:253–271.

MacKay, R. S. (2004). Slow manifolds. In Dauxois, T., Litvak-Hinenzon, A., MacKay, R. S., and Spanoudaki, A., editors, *Energy Localisation and Transfer*, pages 149–192. World Scientific, Singapore.

McIntyre, M. (2015). Dynamical meteorology – balanced flow. In Pyle, J. and Zhang, F., editors, *Encyclopedia of Atmospheric Sciences*, pages 298–303. Academic Press, Oxford, second edition.

McIntyre, M. E. and Norton, W. A. (2000). Potential vorticity inversion on a hemisphere. *J. Atmos. Sci.*, 57(9):1214–1235.

McIntyre, M. E. and Roulstone, I. (2002). Are there higher-accuracy analogues of semi-geostrophic theory? In Norbury, J. and Roulstone, I., editors, *Large-scale atmosphere–ocean dynamics*, volume 2, pages 301–364. Cambridge University Press, Cambridge.

Mohebalhojeh, A. R. and Dritschel, D. G. (2001). Hierarchies of balance conditions for the f-plane shallow-water equations. *J. Atmos. Sci.*, 58(16):2411–2426.

Oliver, M. (2006). Variational asymptotics for rotating shallow water near geostrophy: a transformational approach. *J. Fluid Mech.*, 551:197–234.

Poulin, F. J. (2016). PyRsw: Python rotating shallow water model. GitHub repository, GitHub, commit c504456, https://github.com/PyRsw/PyRsw.

Salmon, R. (1998). *Lectures on Geophysical Fluid Dynamics.* Oxford University Press.

Vallis, G. K. (2017). *Atmospheric and Oceanic Fluid Dynamics: Fundamentals and Large-scale Circulation.* Cambridge University Press.

Vanneste, J. (2013). Balance and spontaneous wave generation in geophysical flows. *Ann. Rev. Fluid Mech.*, 45(1):147–172.

Viúdez, A. and Dritschel, D. G. (2004). Optimal potential vorticity balance of geophysical flows. *J. Fluid Mech.*, 521:343–352.

von Storch, J.-S., Badin, G., and Oliver, M. (2019). The interior energy pathway: inertial gravity wave emission by oceanic flows. In Eden, C. and Iske, A., editors, *Energy Transfers in Atmosphere and Ocean*, pages 53–85. Springer, Cham.

Warn, T., Bokhove, O., Shepherd, T., and Vallis, G. (1995). Rossby number expansions, slaving principles, and balance dynamics. *Quart. J. R. Meteorol. Soc.*, 121(523):723–739.